


**Hybrid nodal surface and nodal line phonons in solids**Wen-Han Dong <sup>1,2</sup>, Jinbo Pan,<sup>1,2,3</sup> Jia-Tao Sun,<sup>4</sup> and Shixuan Du<sup>1,2,3,5,\*</sup><sup>1</sup>*Beijing National Laboratory for Condensed Matter Physics and Institute of Physics, Chinese Academy of Sciences, Beijing 100190, China*<sup>2</sup>*School of Physical Sciences, University of Chinese Academy of Sciences, Beijing 100049, China*<sup>3</sup>*Songshan Lake Materials Laboratory, Dongguan 523808, China*<sup>4</sup>*School of Integrated Circuits and Electronics, MIIT Key Laboratory for Low-Dimensional Quantum Structure and Devices, Beijing Institute of Technology, Beijing 100081, China*<sup>5</sup>*CAS Center for Excellence in Topological Quantum Computation, Beijing 100190, China*

(Received 30 May 2023; revised 25 July 2023; accepted 11 September 2023; published 25 September 2023)

Phonons have provided an ideal platform for a variety of intriguing physical states, such as non-Abelian braiding and the Haldane model. It is promising that phonons will realize the complicated nodal states accompanying unusual quantum phenomena. Here, we propose the hybrid nodal surface and nodal line (NS+NL) phonons beyond the single-genre nodal phonons. We categorize the NS+NL phonons into two- and four-band situations based on symmetry analysis and compatibility relationships. Combining database screening with first-principles calculations, we identify the ideal candidate materials for realizing all categorized NS+NL phonons. Our calculations and tight-binding models further demonstrate that the interplay between NS and NL induces unique phenomena. In space group (SG) 113, the quadratic NL acts as a hub of the Berry curvature between two NSs, generating ribbonlike surface states (SSs). In SG 128, the NS serves as the counterpart of the Weyl NL, in which NS-NL mixed topological SSs are observed. Our findings extend the scope of hybrid nodal states and enrich the phononic states in realistic materials.

DOI: [10.1103/PhysRevB.108.115153](https://doi.org/10.1103/PhysRevB.108.115153)**I. INTRODUCTION**

Nodal semimetals have provided an attractive platform for exploring exotic quantum phenomena since their discovery in electronic systems [1–8]. These gapless states are generally classified as nodal points [9], nodal lines (NLs) [10], and nodal surfaces (NSs) [11,12] according to the degeneracy in their energy-momentum relationships. As compared with electrons, phonons have provided an ideal platform for realizing nodal semimetal states due to their spinless nature and no Fermi level limits, thus promoting the rising field of topological phononics [13,14]. Given the variety of space groups (SGs) and crystalline symmetries, multifarious symmetry-required nodal states have been discovered in phonons, for instance, multiband non-Abelian crossings [15,16], Weyl points [17–20], Dirac points [21], Weyl NLs (WNLs) [22], quadratic NLs (QNLs) [23], hybrid nodal rings [24], nodal nets, nodal chains, and nodal boxes [25–27]. The class-II NS [12] phonons were also predicted, which are subdivided into 1NS, 2NS, and 3NS according to the pairs of NS states [28–31]. Recently, Wang *et al.* [32] reviewed the rapidly expanding fields of NL and NS phonons with a systematic understanding of the classifications of NL phonons and their material realizations. Despite these advances of nodal phonons, however, few researchers have achieved hybrid phonons containing more than one genre of nodal points,

NLs, or NSs so far. It remains elusive whether the hybrid systems host their unique physical phenomena.

Nodal states may exhibit distinctive surface states (SSs) regardless of whether they are topological. For example, the topologically trivial QNL is manifested by torus SSs that span over the surface Brillouin zone [33,34]. Unlike a nodal point or NL, the NS itself creates no SSs since its spatial codimension is zero [12]. One effective approach toward SSs of NSs is to realize the chiral crystals with coexistent NSs and Weyl points [35,36]. Guaranteed by the Nielsen-Ninomiya no-go theorem [37], the NS is topologically charged by Weyl points; hence, one can observe the surface-arc states connecting NSs and Weyl points [35,36]. It was also reported that the NS can possess chiral charges without an upper limit when wrapping multiple Weyl points [38]. Aside from the Weyl point, the NL is another choice to generate SSs of NSs. The NS and NL may coexist in many forms, such as 1NS linked by a straight WNL in the superprismane-carbon [39] and lanternlike phonons in  $\text{Li}_6\text{WN}_4$  [40]. However, these studied systems revealed no SS of a NS but only the drumhead SSs from WNLs. It is of fundamental interest to answer whether NSs and NLs can interplay with each other and induce unique physical states, which is also crucial in understanding hybrid nodal states composed of nodal states with different classifications.

In this paper, we propose hybrid NS and NL (NS+NL) phonons, whose phonon dispersions simultaneously contain NSs and NLs within two bands. We address two main questions: one is the variety of NS+NL phonons, and the other is their distinctive SSs. Based on symmetry analysis and

\*sxdu@iphy.ac.cn

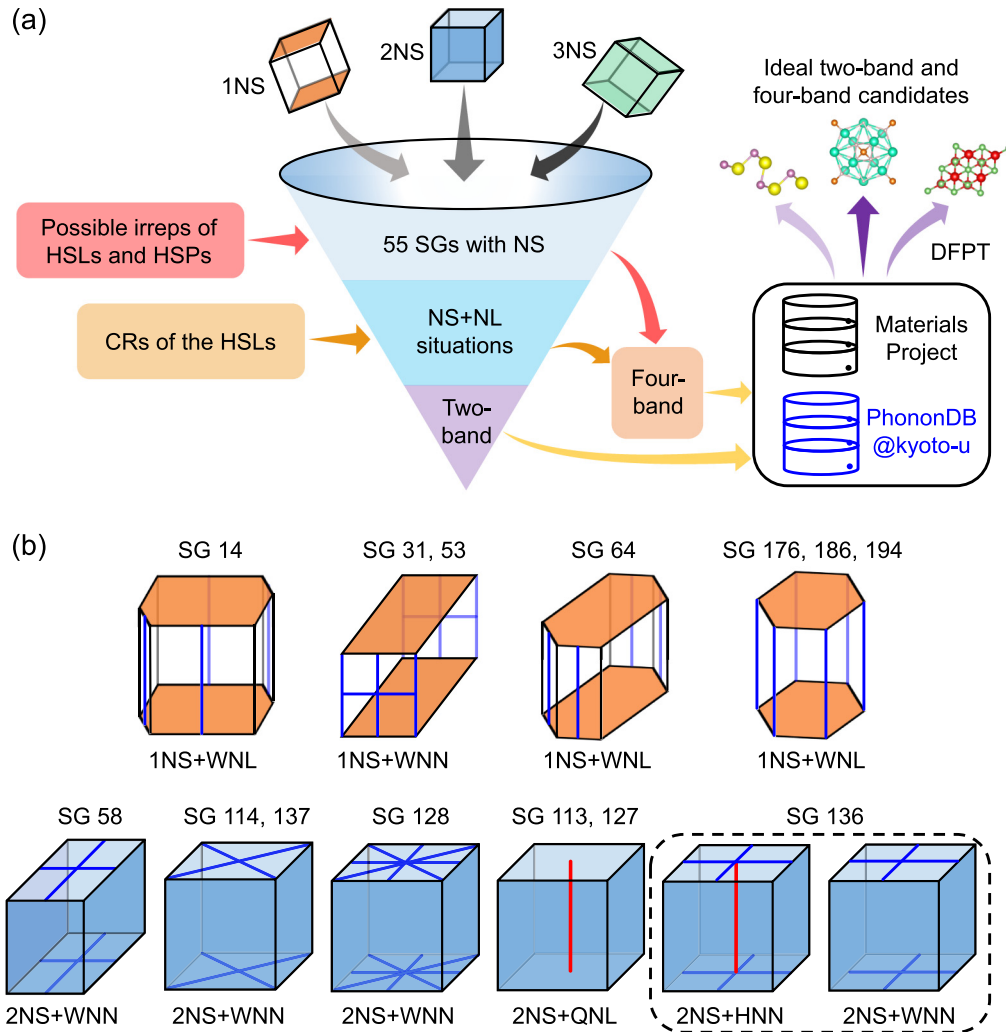


FIG. 1. Catalog of nodal surface and nodal line hybrid (NS+NL) phonons. (a) Workflow for classifying NS+NL phonons and screening ideal candidates from material databases. Here, irrep is irreducible representation, HSL is high-symmetric line, HSP is high-symmetric point, SG is space group, CR is compatibility relationship. I, II, and III stand for three mechanisms of four-band, see Supplemental Material [43] for details. (b) Classifications of two-band NS+NL phonons with their degenerate configurations in the Brillouin zones. The orange and blue surfaces stand for 1NS and 2NS, respectively. The blue and red lines are Weyl NL (WNL) and quadratic NL (QNL), respectively. WNN represents Weyl nodal net, HNN represents hybrid nodal net.

compatibility relationships, we first obtained a complete catalog of the NS+NL phonons in three-dimensional SGs. We subdivided them into two- and four-band situations according to the minimal bands required. Our database screening and first-principles calculations further evidenced that all categorized NS+NL phonons are feasible in realistic materials. Specifically, our calculations and spinless tight-binding (TB) models confirmed both QNLs and WNLs can induce SSs of NSs, reflecting the interplay between NSs and NLs. Our discoveries not only uncover the universality of NS+NL phonons in solids but also offer insight into hybrid nodal states.

## II. CATALOG AND MATERIAL SCREENING

As illustrated in Fig. 1(a), our approach toward NS+NL phonons was to search coexisting NLs in the 55 SGs with symmetry-enforced NSs [28–30]. We focused on NLs

appearing along high-symmetric lines instead of nodal loops or accidentally degenerate NLs. We first inspected all possible irreducible representations of the 55 SGs at high-symmetric points and high-symmetric lines, then checked the compatibility relationships [41] of high-symmetric lines. These two steps ensured a complete consideration of the degeneracy and connectedness of phonon bands in the whole Brillouin zone, i.e., graph theory combinatorics [42]. We adopted the methods of Ref. [23] to determine whether each degenerate line is a WNL or QNL. Finally, we obtained a complete catalog of NS+NL phonons, where the two-band situations are listed in Table I and four-band situations are listed in Supplemental Material (SM) Tables S1–S3 [43]. Figure 1(b) shows the degenerate configurations of two-band NS+NL phonons. It notes that the NLs may constitute different nodal nets [48], such as the Weyl nodal net (WNN) in SG 128 and hybrid nodal net (HNN) composed of both a QNL and WNLs in SG 136. Hence, the two-band NS+NL phonons

TABLE I. Two-band situations of NS+NL phonons<sup>a</sup>.

SG	Symbol	NS	WNL	QNL	Candidate
14	$P2_1$	NS <sub>ZCED</sub>	BD $\{U_1^1 \oplus U_2^1\}$ , AE $\{V_1^1 \oplus V_2^1\}$		mp-4549 SrSiN <sub>2</sub>
31*	$Pmn2_1$	NS <sub>ZURT</sub>	XU $\{G_1^2\}$ , SR $\{Q_1^2\}$ , XS $\{D_1^1 \oplus D_2^1\}$		mp-755543 HoHO <sub>2</sub>
53	$Pmna$	NS <sub>ZURT</sub>	XU $\{G_1^2\}$ , SR $\{Q_1^2\}$ , XS $\{D_1^2\}$		mp-569052 AgSe <sub>3</sub> I
58	$Pnmm$	NS <sub>UXS</sub> , NS <sub>TYS</sub>	ZU $\{A_1^2\}$ , ZT $\{B_1^2\}$		mp-19795 InS
64	$Cmce$	NS <sub>ZRT</sub>	SR $\{D_1^1 \oplus D_2^1\}$		mp-17667 Sr <sub>3</sub> AlSb <sub>3</sub>
113*	$P-42_1m$	2×NS <sub>XRM</sub>		<b>FZ <math>\{LD_3^1 \oplus LD_4^1\}</math></b>	C <sub>4</sub> N [52]
114*	$P-42_1c$	2×NS <sub>XRM</sub>	ZA $\{S_1^1 \oplus S_2^1\}$		mp-27144 TIPO <sub>3</sub>
127	$P4/mbm$	2×NS <sub>XRM</sub>		<b>FZ <math>\{LD_5^2\}</math></b>	mp-29138 KAuSe <sub>2</sub>
128	$P4/mnc$	2×NS <sub>XRM</sub>	ZR $\{U_1^2\}$ , ZA $\{S_1^2\}$		mp-28247 K <sub>2</sub> PtI <sub>6</sub>
136	$P4_2/mnm$	2×NS <sub>XRM</sub>	ZR $\{U_1^2\}$	<b>FZ <math>\{LD_5^2\}</math></b>	mp-3188 ZnSb <sub>2</sub> O <sub>6</sub>
136	$P4_2/mnm$	2×NS <sub>XRM</sub>	ZR $\{U_1^2\}$		mp-662530 KNiPS <sub>4</sub>
137	$P4_2/nmc$	2×NS <sub>XRM</sub>	ZA $\{S_1^2\}$		mp-559639 K <sub>4</sub> UP <sub>2</sub> O <sub>10</sub>
176	$P6_3/m$	NS <sub>ALH</sub>	<b>KH <math>\{P_2^1 \oplus P_3^1\}</math></b>		mp-27506 K <sub>3</sub> W <sub>2</sub> Cl <sub>9</sub>
186*	$P6_3/mc$	NS <sub>ALH</sub>	<b>KH <math>\{P_3^2\}</math></b>		mp-561681 CsSO <sub>3</sub>
194	$P6_3/mmc$	NS <sub>ALH</sub>	<b>KH <math>\{P_3^2\}</math></b>		mp-841 Li <sub>2</sub> O <sub>2</sub>

<sup>a</sup>The required SGs, positions of NS, irreducible representations of NLs, and candidate materials with ideal two-band NS+NL phonons are given. Here, mp-xxx represents the Materials Project [49] ID. Notice the asterisks label noncentrosymmetric SGs. The NLs in bold lines depend on specific basis functions.

take various forms of 1NS+WNL, 2NS+WNL, 2NS+HNN, etc. For four-band situations, we classified them by three different mechanisms, see SM Sec. IV [43] for details. Here, the NS+NL phonons are still identified by their two-band degeneracies, but the minimal bands required for hosting corresponding states, i.e., the dimensionality of elementary band representation [41], are four. Attractively, four-band situations can achieve NS+NL phonons beyond two-band ones, such as the 1NS+QNL+WNL phonons shown in Figs. S37–S41 in the SM [43].

Next, we obtained candidate materials for realizing all categorized NS+NL phonons using high-throughput database screening and first-principles calculations. In detail, we first sought out nearly 200 materials hosting isolated phonon bands and desired SGs from over 10000 *ab initio* phonon records deposited in the Materials Project [49] and Phonon Database at Kyoto University (PhononDB@kyoto-u) [50]. We then checked the irreducible representations and compatibility relations of the database-downloaded phonon data of these materials and performed double-checks by redoing phonon calculations using density functional perturbation theory [51]. We eventually found most candidate materials after database screening and double-checks. The remaining candidates were further identified in the literature and by performing phonon calculations of those materials from the Materials Project [49] that have no phonon data but host specific SGs. As listed in the last columns of Tables I and S1–S3 in the SM

[43], almost all selected candidate materials have been experimentally synthesized and can be found in the Materials Project [49]. To highlight, these candidates all have ideal two- or four-band NS+NL phonon dispersions within a specific frequency range. The two-band NS+NL phonons of candidates listed in Table I are even robust against the longitudinal and transverse optical phonon splitting (LOTO). Collectively, these candidates evidence our proposed NS+NL phonons are feasible in realistic materials. The diversity of NS+NL phonons would induce rich physical states, which we will show in the examples below.

### III. TWO-BAND 2NS+QNL PHONON IN SG 113

When  $\mathcal{P}$  is broken, nonzero Berry curvature can bridge two nodal states, such as the chirality-opposite Weyl points in TaAs [5]. In a similar way, if there only exists a NS and a QNL, the Berry curvature should connect them both. It motivated us to explore the 2NS+QNL phonon in noncentrosymmetric SG 113. As shown in Fig. 2(a), the studied material is a proposed carbonitride C<sub>4</sub>N [52]. Here, C<sub>4</sub>N exhibits a diamondlike structure in SG 113, whose symmetry generators are twofold rotation  $C_{2z}$ , fourfold improper rotation  $S_{4z} = \{C_{4z}\mathcal{P}|0, 0, 0\}$ , and twofold screw rotation  $S_{2y} = \{C_{2y}|\frac{1}{2}, \frac{1}{2}, 0\}$ . Our optimized lattice constants are  $a = b = 3.50$  Å and  $c = 4.88$  Å. The unit cell of C<sub>4</sub>N possesses two  $sp^2$  C, six  $sp^3$  C, and two N atoms. We adopted the unit cell termination with  $sp^2$  C and N atoms.

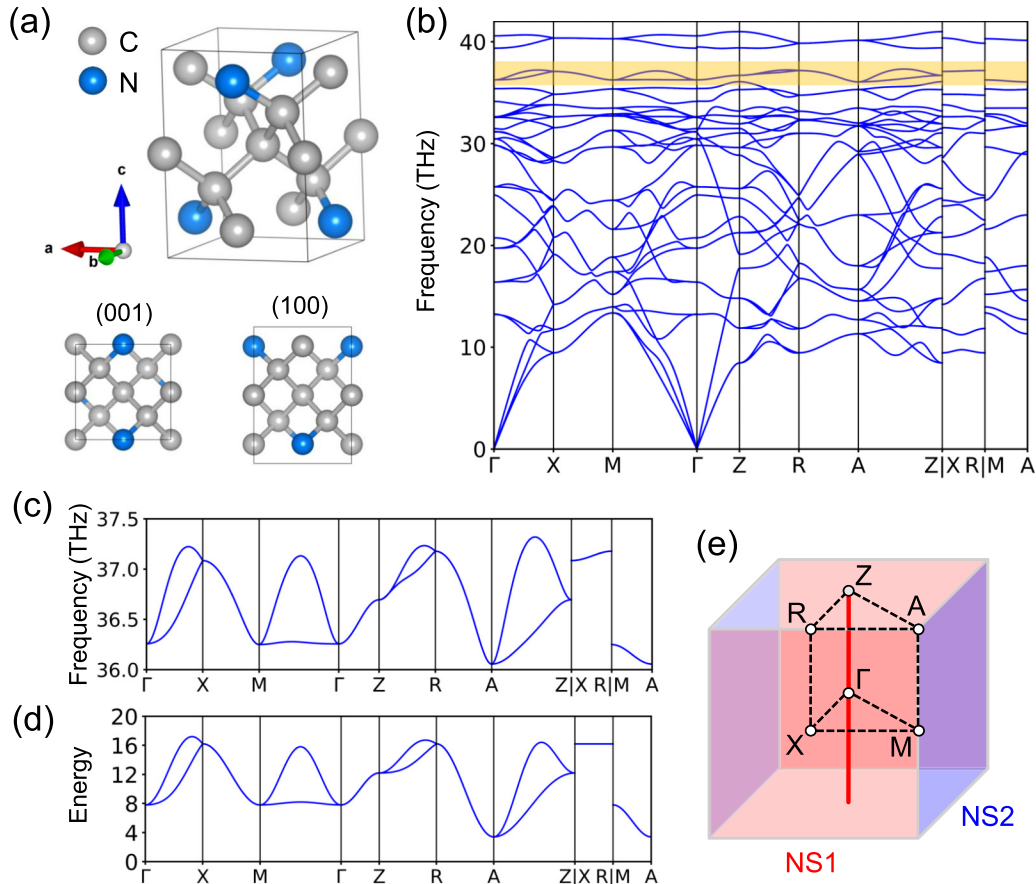


FIG. 2. The 2NS+QNL phonon in SG 113  $C_4N$ . (a) Crystal structure of diamondlike  $C_4N$ . (b) Phonon dispersions of  $C_4N$  with LOTO correction. (c) Phonon bands 27, 28, as marked yellow in (b). (d) Phonon dispersions of the two-band tight-binding (TB) model of SG 113. The TB parameters are  $\Delta = 12.0$ ,  $t_1 = 0.55$ ,  $t_{2\sigma} = -2.0$ ,  $t_{2\pi} = -0.1$ ,  $t_3 = 0.0$ ,  $t_4 = -0.275$ ,  $t_5 = -0.3$ , and  $t_6 = -0.1$  in units of  $t_0$ , and  $z = 0.1$ . (e) Schematic of the Brillouin zone and the 2NS+QNL phonons. The 2NS are divided into NS1 at  $k_x = \pi$  and NS2 at  $k_y = \pi$ .

Figure 2(b) shows the phonon dispersion of  $C_4N$ , which is dynamically stable. Here, we focus on bands 27, 28 with ideal 2NS+QNL dispersions [see Fig. 2(c)]. We distinguish the 2NS as NS1 at  $k_x = \pi$  plane and NS2 at  $k_y = \pi$  plane, as illustrated in Fig. 2(e). Here, NS1 and NS2 are Kramer's degenerate under the joint operation of  $S_{2x,y}$  and time-reversal  $\mathcal{T}$ , where  $\mathcal{T}^2 = 1$  and  $(S_{2x,y}\mathcal{T})^2 = e^{ik_{x,y}} = -1$  in the  $k_{x,y} = \pi$  planes. In SM Sec. III [43], our  $k \cdot p$  analysis and band expansions reveal that NS1 and NS2 are different from the free Weyl NS proposed in Ref. [53]. They have a linear dispersion near the central parts around the  $X$ - $R$  path but a quadratic dispersion near the  $M$ - $A$  path due to the intersection of two NSs. We then turn to the QNL along the  $\Gamma$ - $Z$  path, whose twofold degeneracy is ensured by an irreducible representation of  $LD_3 \oplus LD_4$ . We have calculated the Berry phase along a closed loop surrounding the QNL:  $\gamma_L = \sum_{n \in \text{occ}} \oint A_n(\mathbf{k}) \cdot d\mathbf{k} \text{ mod } 2\pi$ , where  $A_n(\mathbf{k}) = i\langle u_n(\mathbf{k}) | \nabla_{\mathbf{k}} | u_n(\mathbf{k}) \rangle$  is the Berry connection of the  $n$ th band. The obtained Berry phase of zero indicates the QNL is topologically trivial. Additionally, our  $k \cdot p$  analysis confirms the quadratic effective Hamiltonian near QNL, and the QNL is protected by  $S_{4z}\mathcal{T}$  [43]. In Fig. S4 in the SM [43], we demonstrate the elementary band representation of bands 27, 28 of  $C_4N$  is  $B1@2c$  or  $B2@2c$ . With this knowledge, we further constructed a two-band TB model using the  $p_{xy}$  and  $p_{-xy}$  orbitals locating at

$2c$  Wyckoff positions, see Eqs. (S2)–(S4) and Fig. S1 in the SM [43] for details. Figure 2(d) shows our TB model captures well the dispersion feature of 2NS+QNL phonon in  $C_4N$ .

Physically, the QNL is like a charge-neutral metal rod, and two NSs are analogous to metal plate capacitors. What will happen if one puts the QNL between two NSs? In Fig. 3, we reveal the Berry-curvature-driven SSs of the 2NS+QNL phonon. First, Fig. 3(a) shows the Berry curvature  $\Omega(\mathbf{k})$  of band 27 of  $C_4N$ , which is almost confined in the  $k_x$ - $k_y$  plane. Since  $\mathcal{P}$  is broken and  $\mathcal{T}$  is reserved,  $\Omega(\mathbf{k})$  is nonzero everywhere. Here,  $S_{4z}$  guarantees NS1 and NS2 carry opposite Berry flux, so that NS1 acts like a source and NS2 acts like a sink. We estimated the Berry flux of  $1.8\pi/-1.8\pi$  for NS1/NS2 by integrating the Berry curvature passing through left and right sides of NS1 (NS2). Interestingly, though the QNL carries a net flux of zero, it absorbs the Berry flux from the central part of NS1 and emits it to NS2. This hublike behavior of QNL blocks the direct exchange of the Berry flux between the central parts of NS1 and NS2, generating a crosslike barrier along  $[110]$  and  $[\bar{1}\bar{1}0]$  directions near the  $\Gamma$ - $Z$  path. In Fig. 3(b), our TB model reproduces the unique NS1-QNL-NS2 distribution of the Berry curvature. The minor difference between Figs. 3(a) and 3(b) may come from TB model simplification.



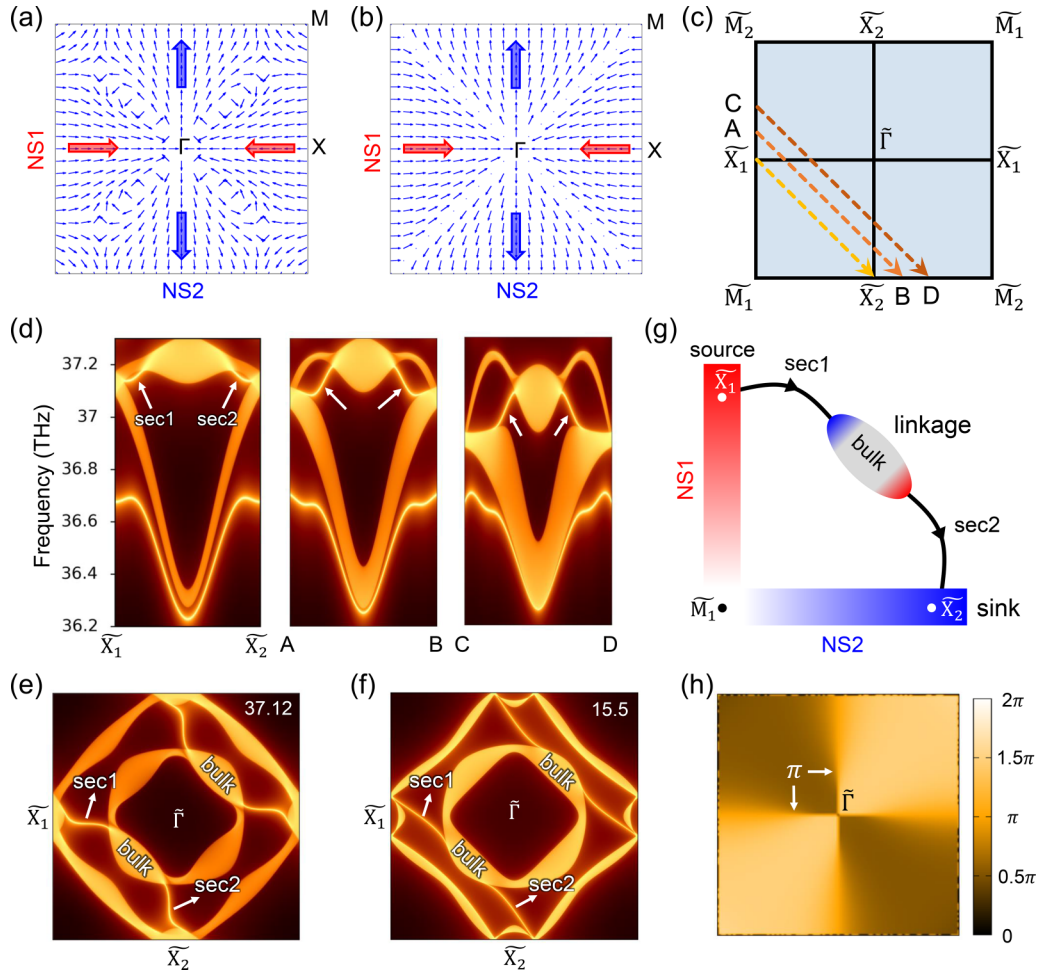


FIG. 3. Ribbonlike surface states (SSs) of the 2NS+QNL phonons. (a) In-plane Berry curvature  $\Omega_{x,y}(\mathbf{k})$  of band 27 of  $C_4N$  at  $k_z = 0$ . (b) In-plane Berry curvature  $\Omega_{x,y}(\mathbf{k})$  of the tight-binding (TB) model at  $k_z = 0$ . (c) Schematic of the (001) surface Brillouin zone. (d) Surface spectra of  $C_4N$  along the paths labeled in (c). The arrows point to the two sections of SSs, namely, sec 1 and sec 2, which are stabilized by intermediate bulk states. (e) The isofrequency (001) surface contour of  $C_4N$  at 37.12 THz. (f) The isofrequency (001) surface contour of TB model at  $E = 15.5t_0$ . (g) Schematic of the ribbonlike SSs at a fixed frequency, where red (blue) represents positive (negative) Berry flux. If one considers the SSs at different frequencies collectively, they constitute the ribbon. (h) Calculated Zak phase  $\mathcal{Z}(k_x, k_y)$  up to band 27 of  $C_4N$ .

Next, we investigate the SSs induced by Berry curvature. Since NS1 and NS2 resemble a pair of source and sink, such SSs should appear in between the projections of two NSs. Figure 3(d) shows the (001) surface spectra of  $C_4N$  along the NS1-to-NS2 paths, as arrowed in Fig. 3(c). One can find the torus SSs of QNL [33] emerge between 36.0 and 36.7 THz (see also Fig. S7 in the SM [43]). Our concerned SSs locate between the bulk gaps, consisting of two sections, i.e., sec 1 and sec 2. To distinguish, we term them as ribbonlike SSs and will explain below. Figure 3(e) shows the isofrequency (001) surface contour of  $C_4N$  at 37.12 THz. The ribbonlike SSs start from NS1, are then bridged by intermediate bulk states, and finally end at NS2. Figure 3(g) illustrates that the SSs are driven by the nonzero Berry flux of NS1 and NS2. The SSs follow the direction of the Berry curvature from NS1 to NS2. Notice each SS is separated by the intermediate bulk states into two sections, possibly because the Berry curvature cannot directly connect the central parts of NS1 and NS2. We discuss in Fig. S6 in the SM [43] that the intermediate bulk states are crucial in

stabilizing the SSs because NS1 and NS2 are connected without a global gap. In Fig. S6 in the SM [43], we also show the ribbonlike SSs appear in a wide range between 36.88 and 37.14 THz. With this knowledge, we illustrate that the SSs under different frequencies (momenta) collectively occupy the surface Brillouin zone like ribbons, i.e., these SSs are ribbonlike. We remark that the ribbonlike SSs do not come from topological charge of NS; instead, they are driven by the Berry curvature between 2NS and QNL. The QNL is essential in creating the indirectly connected SSs between 2NSs because the 2NSs have a codimension of zero, and the zero-dimensional charge in bulk generates no SS itself [12,54]. We verify this point in Fig. S8 in the SM [43] that the SS will disappear if there only exist 2NSs without a QNL. To further confirm the above results of  $C_4N$ , we have also obtained the ribbonlike SSs with two sections using the TB model, as shown in Fig. 3(f).

Lastly, we revisit the ribbonlike SSs from the perspective of the Zak phase. The Zak phase of the (001) surface is defined as the one-dimensional Berry phase along the  $k_z$

axis [55]:  $\mathcal{Z}(k_x, k_y) = \sum_{n \in \text{occ}} \int_{-\pi}^{\pi} A_n^z(\mathbf{k}) dk_z$ . Figure 3(h) shows the calculated Zak phase up to band 27 of  $C_4N$ . Notice  $S_{4z}$  and glide mirrors  $\tilde{\mathcal{M}}_{\pm xy} = \{\mathcal{M}_{\pm xy} | \frac{1}{2}, \frac{1}{2}, 0\}$  ensure  $\mathcal{Z}(k_x, k_y) = -\mathcal{Z}(-k_y, k_x) = \mathcal{Z}(k_y, k_x) = \mathcal{Z}(-k_y, -k_x) \pmod{2\pi}$ , which gives the 0 or  $\pi$  quantized Zak phase along  $k_x = 0$  and  $k_y = 0$ . For  $C_4N$  in Fig. 3(h), one can clearly see the Zak phase is nonzero in the whole surface Brillouin zone. In modern theory of electrical polarization, the nonzero Zak phase reveals accumulative surface polarization charge from the bulk [56]. Given the considerable Zak phase value between  $0.45\pi$  and  $1.55\pi$ , it indicates a wide distribution of SSs in the (001) surface of  $C_4N$  [57]. The  $\pi$ -quantized Zak phase along  $k_x = 0$  and  $k_y = 0$  helps explain why the stable SSs incline to appear around  $\tilde{\Gamma}-\tilde{X}_1$  and  $\tilde{\Gamma}-\tilde{X}_2$  paths. Moreover, we show the relation between the Zak phase and Berry curvature:  $\mathcal{Z}(k_x, k_y) - \mathcal{Z}(k'_x, k'_y) = \sum_{n \in \text{occ}} \oint A_n(\mathbf{k}) \cdot d\mathbf{C} = \sum_{n \in \text{occ}} \iint \Omega(\mathbf{k}) \cdot d\mathbf{S} \pmod{2\pi}$ , where  $(k_x, k_y)$  and  $(k'_x, k'_y)$  are arbitrary points, and  $\mathbf{S}$  is the closed area with boundary  $\mathbf{C}: (k_x, k_y, \pi) \rightarrow (k'_x, k'_y, \pi) \rightarrow (k'_x, k'_y, -\pi) \rightarrow (k_x, k_y, -\pi) \rightarrow (k_x, k_y, \pi)$ . In this sense, the Berry flux from  $\mathcal{P}$  breaking creates the considerable Zak phase in the whole surface Brillouin. The  $\pi$ -quantized Zak phase locally protects the ribbonlike SSs around  $k_x = 0$  and  $k_y = 0$ . This Berry-curvature-based physics is quite different from that of Weyl points, revealing the uniqueness of ribbonlike SSs between the NS and QNL.

#### IV. TWO-BAND 2NS+WNN PHONON IN SG 128

In addition to generating SSs between NSs and QNLs, NSs may appear as the counterpart of WNLs and give rise to nontrivial SSs. Here, we choose the example of a 2NS+WNN phonon in SG 128 to verify this point. The studied material is  $K_2PtI_6$ , which was synthesized using solution methods [58]. Here,  $K_2PtI_6$  is crystallized in SG 128, whose structure is shown in Fig. 4(a). The symmetry generators are fourfold rotation  $C_{4z}$ , twofold screw rotation  $S_{2y} = \{C_{2y} | \frac{1}{2}, \frac{1}{2}, \frac{1}{2}\}$ , and  $\mathcal{P}$ . Our optimized lattice constants are  $a = b = 7.73 \text{ \AA}$  and  $c = 12.13 \text{ \AA}$ . Figure 4(b) shows the phonon dispersion of  $K_2PtI_6$  with LOTO correction, within which bands 43, 44; bands 45, 46; and bands 47, 48 exhibit ideal 2NS+WNN phonons. It is noted that any isolated two bands can host such a 2NS+WNN phonon since it is symmetry enforced.

We take bands 43, 44 of  $K_2PtI_6$  for investigating the 2NS+WNN phonon [see Fig. 4(c)]. Figure 4(d) displays that bands 43, 44 have 2NS in the  $k_{x,y} = \pi$  planes and WNN in the  $k_z = \pi$  plane. From previous discussions, the two NSs are enforced by  $S_{2x,y}\mathcal{T}$ . One cannot directly define the topological charge of a NS due to its connection with the WNN. The WNN is formed by two WNLs along Z-A paths and two WNLs along Z-R paths. The WNLs along Z-R paths are protected by the anticommutation relations:  $\{\mathcal{M}_z, \tilde{\mathcal{M}}_{x,y}\} = 0$  and  $\{\mathcal{M}_z, S_{2x,y}\} = 0$ , where  $\mathcal{M}_z$  is the perpendicular mirror and  $\tilde{\mathcal{M}}_{x,y} = \{\mathcal{M}_{x,y} | \frac{1}{2}, \frac{1}{2}, \frac{1}{2}\}$  are glide mirrors. The WNLs along Z-A paths are protected by  $\{\mathcal{M}_z, \tilde{\mathcal{M}}_{\pm xy}\} = 0$  and  $\{\mathcal{M}_z, S_{2(\mp xy)}\} = 0$ , where  $\tilde{\mathcal{M}}_{\pm xy} = \{\mathcal{M}_{\pm xy} | \frac{1}{2}, \frac{1}{2}, \frac{1}{2}\}$  and  $S_{2(\mp xy)} = \{C_{2(\mp xy)} | \frac{1}{2}, \frac{1}{2}, \frac{1}{2}\}$ . Additionally, we have determined the topological charge of these WNLs by calculating the Berry phases  $\gamma_L$  using closed loops away from the Z point and 2NS. We obtained the nontrivial  $\gamma_L = \pi$ , which is quantized by  $\mathcal{M}_z$ .

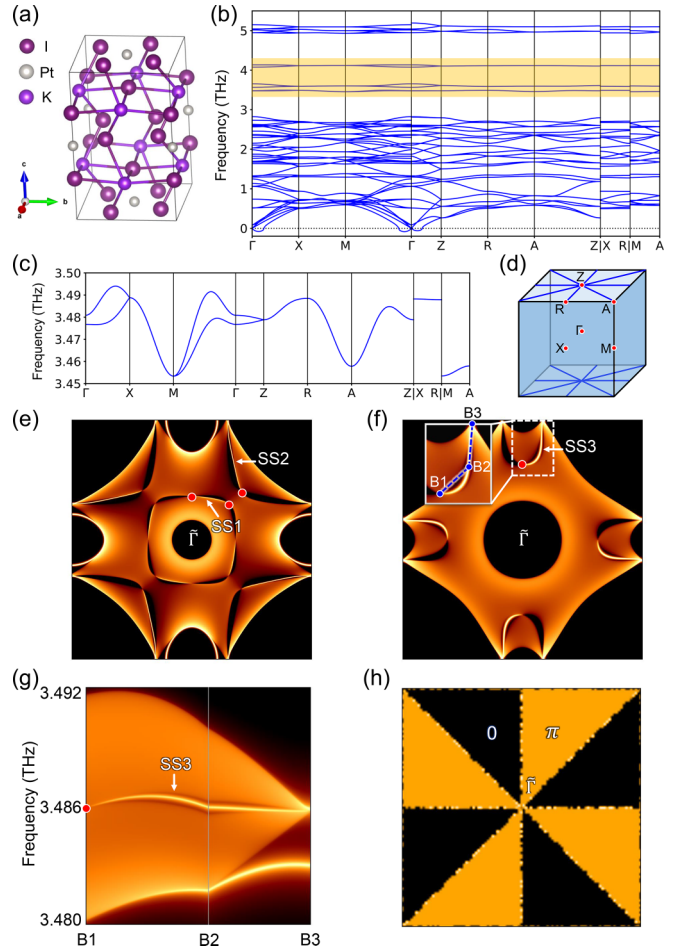


FIG. 4. The 2NS+WNN phonons in SG 128  $K_2PtI_6$ . (a) Crystal structure of  $K_2PtI_6$  (mp-28247). (b) Phonon dispersions of  $K_2PtI_6$  with LOTO correction. Bands 43, 44, bands 45, 46 and bands 47, 48 are marked by yellow, which respectively exhibits ideal two-band 2NS+WNN phonons. (c) Zoom-in view of bands 43, 44. (d) Schematic of the Brillouin zone and the 2NS+WNN phonon of bands 43, 44. The isofrequency contours of (001) surface at (e) 3.4822 THz and (f) 3.486 THz. SS1, SS2, and SS3 are topological SSs from either WNL to WNL or NS to WNL. (g) (001) surface spectrum of the  $K_2PtI_6$  along projections of WNL to NS. The path is shown in inset of (f). (h) Calculated Zak phase  $\mathcal{Z}(k_x, k_y)$  of (001) surface up to band 43.

Figures 4(e) and 4(f) exhibit the SSs of  $K_2PtI_6$  at different frequencies. We find three kinds of topological SSs, i.e., SS1 from WNL of the Z-A path to WNL of the Z-R path, SS2 from WNL of the Z-A path to one NS and SS3 from WNL of the Z-R path to one NS. Figure 4(g) shows the (001) surface spectrum that SS3 starts from a WNL and ends into NS projections. Here, SS2 and SS3 are topological SSs between NSs and WNLs. Also, SS2 and SS3 are quite different from SS1 in that their terminations near the NS projections are not simple points. Considering the NS cannot generate topological charge by itself, it means such NS-WNL SSs have their unique formation mechanism, which we will discuss below. Then we demonstrate the topological nature of SS1, SS2, and SS3. Figure 4(h) displays the (001) Zak phase distribution up to band 43 of  $K_2PtI_6$ . The Zak phase undergoes a jump of

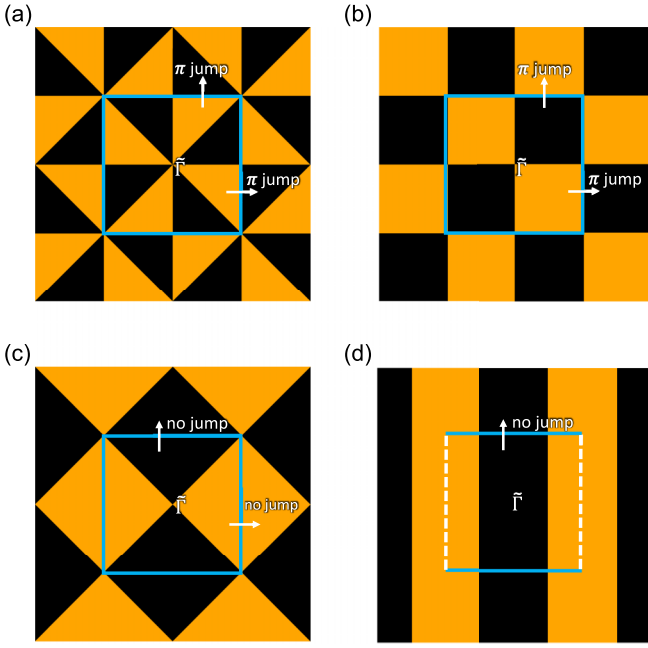


FIG. 5. Determining the NS-WNL mixed topological SSs in centrosymmetric SGs by Zak phase. (a) (001) Zak phase of 2NS+WNN phonon in SG 128. (b) (001) Zak phase of 2NS+WNN phonons in SG 58 and SG 136. The (100) Zak phase of 1NS+WNN phonon in SG 53 is like (b). (c) (001) Zak phase of 2NS+WNN phonon in SG 137. (d) (100) Zak phase of 1NS+WNL phonons in SG 14, SG 64, SG 176, and SG 194. Here, the cyan boxes (lines) represent projections of NS. The gold and black regions are separated from either other by the projection of WNL or NS, exhibiting quantized Zak phase of 0 and  $\pi$ , respectively.

$\pi$  once it crosses the projection of WNL. Here,  $\mathcal{P}$  ensures that  $\mathcal{Z}(k_x, k_y)$  is quantized to either 0 or  $\pi$ . Eventually, the  $\mathcal{Z}(k_x, k_y) = \pi$  and  $\mathcal{Z}(k_x, k_y) = 0$  regions each occupy half of the (001) surface. Here, SS1, SS2, and SS3 are topologically nontrivial because they appear in the  $\mathcal{Z}(k_x, k_y) = \pi$  regions. Furthermore, we have constructed a two-band TB model to describe the 2NS+WNN phonon in SG 128, see Eqs. (S7)–(S10) in the SM [43] for details. In Fig. S2 of the SM [43], we reproduce the WNL-WNL SS1 and NS-WNL mixed SS2, SS3 using our TB model, which is consistent with the results of  $\text{K}_2\text{PtI}_6$ .

### V. ORIGIN OF NS-WNL MIXED TOPOLOGICAL SS

Most importantly, we discuss about the formation mechanism of NS-WNL mixed topological SSs. Figure 5 shows the schematics of Zak phases of all possible two-band NS+WNL phonons in centrosymmetric SGs. The Zak phase is defined in the (001) surface for 2NS+WNN phonons and the (100) surface for 1NS+WNL or 1NS+WNN phonons. Notice the (100) Zak phase  $\mathcal{Z}(k_y, k_z)$  is integrated along the  $k_x$  axis. Due to  $\mathcal{P}$ , the Zak phase is quantized to 0 or  $\pi$ . We define  $\mathcal{N}$  as the number of times to pass through the projection of WNL when travelling from one side of NS to the other. We begin with the 2NS+WNN phonon in SG 128. Figure 5(a) shows the Zak phase must have a jump of  $\pi$  when it crosses the projection of the NS at the surface Brillouin zone boundaries. It is because the Zak phase has already been altered

by  $\pi$  three times due to  $\mathcal{N} = 3$ . In this sense, the NS plays the same role as the WNL in the (001) surface and exists as the counterpart of the WNL. The NS at  $k_x = \pi$  ( $k_y = \pi$ ) equivalently carries a Berry phase of  $\pi$ . Hence, the NS-WNL mixed SSs are topologically protected in SG 128, as observed in  $\text{K}_2\text{PtI}_6$ . Figure 5(b) shows such a physical image is also applicable for  $\mathcal{N} = 1$  cases, e.g., the 1NS+WNN phonon in SG 53 and 2NS+WNN phonons in SG 58 and SG 136. Taking SG 53 as an example, we have investigated the 1NS+WNN phonon using both a TB model and realistic material  $\text{AgSe}_3\text{I}$  [59]. The results evidence the existence of NS-WNL mixed SSs as well as WNL-WNL SSs (see Figs. S3, S11, and S12 in the SM [43]). In addition, we demonstrate the  $\mathcal{N} = 2$  and 0 cases cannot host NS-WNL mixed SSs because the NS equivalently carries no topological charge [see Figs. 5(c) and 5(d)]. This explains why previous researchers exploring, e.g., superprismane-carbon in SG 194 ( $\mathcal{N} = 0$ ) [39] and  $\text{Li}_6\text{WN}_4$  in SG 137 ( $\mathcal{N} = 2$ ) [40], only found topological SSs between WNLs. In our example of  $\text{Li}_2\text{O}_2$  in SG 194 ( $\mathcal{N} = 0$ ), we illustrate the NS cannot form SSs, and there only exist drum-head SSs between WNLs (see Fig. S25 in the SM [43]). In short, all these demonstrate the topological nature of the NS is determined by the arrangements of WNLs. The NS-WNL mixed SSs appear when  $\mathcal{N}$  is odd.

For better understanding the interplay between NSs and WNLs, we provide a more intrinsic viewpoint that the NS-WNL interaction depends on whether the NS is physically equivalent to the WNL in subspace, in other words, whether the NS can degenerate into a WNL under certain perturbations. For the cases with NS-WNL interaction, e.g., the 2NS+WNN phonon of SG 128 ( $\mathcal{N} = 3$ ), supposing the perturbations with breaking twofold screw rotations, one can find the NS degenerates into the WNL locating at the  $A$ - $R$  path since the anticommutation relation  $\{\mathcal{M}_z, \mathcal{M}_{x,y}\} = 0$  is still reserved. It means the NS is equivalent to the WNL in subspace. Therefore, the interaction between NSs and WNLs are allowed in these cases. For the cases without NS-WNL interaction, e.g., the 2NS+WNN phonon of SG 137 ( $\mathcal{N} = 2$ ), one can check the NS is completely gapped under the perturbation that breaks twofold screw rotations. It means the NS is not equivalent to any WNL in subspace, so that the NS-WNL interaction is not allowed in these cases.

### VI. FOUR-BAND NS+NL PHONONS

In SM Sec. IV [43], we discuss the four-band NS+NL phonons as categorized in Fig. 1(a). The four bands are caused by three mechanisms: (I) symmetry-enforced fourfold Dirac points or Dirac NLs, (II) Dirac points induced by paired NLs, and (III) hourglass phonons caused by the violation of compatibility relationship. In four-band situations, the NS+NL phonons appear in either the upper or lower two bands of the four bands, i.e., the NS+NL phonons are valid at  $\frac{1}{4}$  or  $\frac{3}{4}$  filling of the four bands. Additionally, the Dirac points, Dirac NLs, or hourglass phonons are at  $\frac{1}{2}$  filling. We show the material candidates of Figs. S26–S44 in the SM [43]. For example, in Fig. S39 of the SM [43],  $\text{Ta}_3\text{SeI}_7$  of SG 186 [60] hosts a pair of 1NS+QNL+WNL phonons in bands 61, 62 and bands 63, 64. The paired QNLs further induce a fourfold Dirac point at the  $A$  point (mechanism II), exhibiting double



surface arcs at the (100) surface. In brief, these four-band cases not only enrich the genres of NS+NL phonons but also intertwine NS+NL phonons with Dirac points [21,61], Dirac NLs [62], and hourglass phonons [63–65], which are promising for realizing much more intriguing nodal states.

## VII. DISCUSSION AND CONCLUSIONS

Before closing, we would like to make some important remarks on our work. First, our symmetry analysis and candidate materials reveal the discovered NS+NL phonons are ubiquitous in solids. If satisfying the symmetries, these NS+NL states are obtainable in other spinless systems, such as acoustic metamaterials and photonic lattices. It means, in this paper, we offer broad opportunities to investigate the hybrid nodal states and their SSs. Second, we reveal the distinctive interplay/interaction between NSs and NLs. For NSs and QNLs, their interplay is reflected by the Berry-curvature-driven ribbonlike SSs. For NSs and WNLs, their interplay gives rise to the NS-WNL mixed topological SSs. These findings go beyond the understandings of single-genre nodal points, NLs, or NSs, thus distinguish our work from recent high-throughput studies on topological/nodal phonons [66,67]. Third, NS+NL phonons may have interesting physical effects and practical applications. For bulk NS+NL phonons, they can exhibit excellent phonon transport properties due to the high degeneracy. In a wide frequency range near the NS or NL, these gapless phonons can greatly increase the scattering centers and strengthen the phonon-phonon scattering processes [68], which reduces the lattice thermal conductivity ( $\kappa_L$ ) by lowering phonon relaxation time [69]. The low  $\kappa_L$  means materials hosting NS+NL phonons are promising for high-performance thermoelectric applications. For surface NS+NL phonons, they have large density of states at boundaries, which may enhance the electron-phonon-interaction-related phenomena [70,71], such as interfacial high- $T_C$  superconductivity [72]. Particularly, the NS-related SSs have open constant-frequency contours, which are desirable for realizing negative refraction at interfaces [73]. For  $\mathcal{P}$ -breaking systems, their SSs are also applicable for valley-based interfacial phononic devices, such as waveguides [74] and antennas [75]. Overall, the various NS+NL phonons and their SSs offer an attractive platform for future research and applications of nodal phonons.

Despite the broad prospects, one should notice it remains challenging to experimentally observe these NS+NL

phonons. First, it requires high-resolution techniques to detect bulk NS+NL phonons. Authors of previous studies have applied inelastic x-ray scattering to detect nodal phonons in FeSi and MoB<sub>2</sub> [76,77]. This meV-resolved technique is not suitable for detecting NS+NL phonons if their band degeneracies appear within a narrow frequency range. Instead, methods like ultrasensitive infrared spectroscopy [78] and high-resolution resonant impulsive stimulated Raman spectroscopy [79] should be much more effective. Second, the intrinsic SSs of NS+NL phonons may be buried in bulk states or exhibit weak transport signals due to surface defects and other material-specific trivial states. This issue can be overcome by fabricating material samples with high-quality surfaces or constructing artificial acoustic lattices as an alternative. We suggest the atomic-resolved techniques like phonon laser [80] and electron energy loss spectroscopy [81] to be applied for detecting the SSs. We expect these discussions can promote the experimental realizations of NS+NL phonons in the near future.

In summary, we propose the NS+NL phonons in three-dimensional SGs and provide a complete classification based on symmetry analysis and compatibility relationships. We identify the candidate materials with ideal two- and four-band NS+NL phonons through database screening and first-principles calculations. Particularly, the two-band candidates are robust against LOTO. Our calculations and spinless TB models together confirm the unique interactions between NSs and NLs, including ribbonlike SSs of the 2NS+QNL phonon in SG 113, and NS-WNL mixed topological SSs in SGs represented by SG 128. Our results not only theoretically extend the scope of hybrid nodal states with a deeper understanding but also offer plentiful realistic materials for experimental applications.

## ACKNOWLEDGMENTS

We thank Dr. Zhongjia Chen, Prof. Hongming Weng, and Prof. Feng Liu for their helpful discussions. This paper was supported by the National Key Research and Development Program of China (Grant No. 2020YFA0308800), the National Natural Science Foundation of China (Grants No. 11974045 and No. 61888102), and Chinese Academy of Sciences (Grant No. XDB30000000). We acknowledge computational support from the National Superconducting Center in Guangzhou.

- 
- [1] A. A. Burkov, M. D. Hook, and L. Balents, *Phys. Rev. B* **84**, 235126 (2011).
  - [2] C. Fang, M. J. Gilbert, X. Dai, and B. A. Bernevig, *Phys. Rev. Lett.* **108**, 266802 (2012).
  - [3] Z. Wang, Y. Sun, X.-Q. Chen, C. Franchini, G. Xu, H. Weng, X. Dai, and Z. Fang, *Phys. Rev. B* **85**, 195320 (2012).
  - [4] A. A. Soluyanov, D. Gresch, Z. Wang, Q. Wu, M. Troyer, X. Dai, and B. A. Bernevig, *Nature (London)* **527**, 495 (2015).
  - [5] H. Weng, C. Fang, Z. Fang, B. A. Bernevig, and X. Dai, *Phys. Rev. X* **5**, 011029 (2015).
  - [6] A. A. Burkov, *Nat. Mater.* **15**, 1145 (2016).
  - [7] Z.-M. Yu, Z. Zhang, G.-B. Liu, W. Wu, X.-P. Li, R.-W. Zhang, S. A. Yang, and Y. Yao, *Sci. Bull.* **67**, 375 (2022).
  - [8] A. C. Potter, I. Kimchi, and A. Vishwanath, *Nat. Commun.* **5**, 5161 (2014).
  - [9] N. P. Armitage, E. J. Mele, and A. Vishwanath, *Rev. Mod. Phys.* **90**, 015001 (2018).



- [10] C. Fang, Y. Chen, H.-Y. Kee, and L. Fu, *Phys. Rev. B* **92**, 081201(R) (2015).
- [11] Q.-F. Liang, J. Zhou, R. Yu, Z. Wang, and H. Weng, *Phys. Rev. B* **93**, 085427 (2016).
- [12] W. Wu, Y. Liu, S. Li, C. Zhong, Z.-M. Yu, X.-L. Sheng, Y. X. Zhao, and S. A. Yang, *Phys. Rev. B* **97**, 115125 (2018).
- [13] Z. Yang, F. Gao, X. Shi, X. Lin, Z. Gao, Y. Chong, and B. Zhang, *Phys. Rev. Lett.* **114**, 114301 (2015).
- [14] Y. Liu, X. Chen, and Y. Xu, *Adv. Funct. Mater.* **30**, 1904784 (2020).
- [15] B. Jiang, A. Bouhon, Z.-K. Lin, X. Zhou, B. Hou, F. Li, R.-J. Slager, and J.-H. Jiang, *Nat. Phys.* **17**, 1239 (2021).
- [16] B. Peng, A. Bouhon, B. Monserrat, and R.-J. Slager, *Nat. Commun.* **13**, 423 (2022).
- [17] J. Liu, W. Hou, E. Wang, S. Zhang, J.-T. Sun, and S. Meng, *Phys. Rev. B* **100**, 081204(R) (2019).
- [18] Q.-B. Liu, Y. Qian, H.-H. Fu, and Z. Wang, *NPJ Comput. Mater.* **6**, 95 (2020).
- [19] Q.-B. Liu, Z. Wang, and H.-H. Fu, *Phys. Rev. B* **103**, L161303 (2021).
- [20] G. Ding, F. Zhou, Z. Zhang, Z.-M. Yu, and X. Wang, *Phys. Rev. B* **105**, 134303 (2022).
- [21] Z. J. Chen, R. Wang, B. W. Xia, B. B. Zheng, Y. J. Jin, Y.-J. Zhao, and H. Xu, *Phys. Rev. Lett.* **126**, 185301 (2021).
- [22] J. Li, Q. Xie, J. Liu, R. Li, M. Liu, L. Wang, D. Li, Y. Li, and X.-Q. Chen, *Phys. Rev. B* **101**, 024301 (2020).
- [23] G. Liu, Y. Jin, Z. Chen, and H. Xu, *Phys. Rev. B* **104**, 024304 (2021).
- [24] Z. J. Chen, Z. J. Xie, Y. J. Jin, G. Liu, and H. Xu, *Phys. Rev. Mater.* **6**, 034202 (2022).
- [25] F. Zhou, H. Chen, Z.-M. Yu, Z. Zhang, and X. Wang, *Phys. Rev. B* **104**, 214310 (2021).
- [26] G. Ding, T. Sun, and X. Wang, *Phys. Chem. Chem. Phys.* **24**, 11175 (2022).
- [27] J. Zhu, W. Wu, J. Zhao, H. Chen, L. Zhang, and S. A. Yang, *npj Quantum Mater.* **7**, 52 (2022).
- [28] Q.-B. Liu, Z.-Q. Wang, and H.-H. Fu, *Phys. Rev. B* **104**, L041405 (2021).
- [29] C. Xie, H. Yuan, Y. Liu, X. Wang, and G. Zhang, *Phys. Rev. B* **104**, 134303 (2021).
- [30] C. Xie, H. Yuan, Y. Liu, and X. Wang, *Phys. Rev. B* **105**, 054307 (2022).
- [31] Y. Liu, N. Zou, S. Zhao, X. Chen, Y. Xu, and W. Duan, *Nano Lett.* **22**, 2120 (2022).
- [32] X. Wang, T. Yang, Z. Cheng, G. Surucu, J. Wang, F. Zhou, Z. Zhang, and G. Zhang, *Appl. Phys. Rev.* **9**, 041304 (2022).
- [33] Z.-M. Yu, W. Wu, X.-L. Sheng, Y. X. Zhao, and S. A. Yang, *Phys. Rev. B* **99**, 121106(R) (2019).
- [34] Z. Zhang, Z.-M. Yu, and S. A. Yang, *Phys. Rev. B* **103**, 115112 (2021).
- [35] Y. Yang, J.-P. Xia, H.-X. Sun, Y. Ge, D. Jia, S.-Q. Yuan, S. A. Yang, Y. Chong, and B. Zhang, *Nat. Commun.* **10**, 5185 (2019).
- [36] M. Xiao, L. Ye, C. Qiu, H. He, Z. Liu, and S. Fan, *Sci. Adv.* **6**, eaav2360 (2020).
- [37] H. B. Nielsen and M. Ninomiya, *Nucl. Phys. B* **185**, 20 (1981).
- [38] J. Z. Ma, S. N. N. Radovic, J. P. Song, Q. S. Wu, S. A. Ekahana, M. Naamneh, M. Radovic, V. N. Strocov, S. Y. Gao, T. Qian *et al.*, *Phys. Rev. B* **105**, 115118 (2022).
- [39] Q.-B. Liu, Z.-Q. Wang, and H.-H. Fu, *Mater. Today Phys.* **24**, 100694 (2022).
- [40] X. Wang, F. Zhou, T. Yang, M. Kuang, Z.-M. Yu, and G. Zhang, *Phys. Rev. B* **104**, L041104 (2021).
- [41] B. Bradlyn, L. Elcoro, J. Cano, M. G. Vergniory, Z. Wang, C. Felser, M. I. Aroyo, and B. A. Bernevig, *Nature (London)* **547**, 298 (2017).
- [42] J. Kruthoff, J. de Boer, J. van Wezel, C. L. Kane, and R.-J. Slager, *Phys. Rev. X* **7**, 041069 (2017).
- [43] See Supplemental Material at <http://link.aps.org/supplemental/10.1103/PhysRevB.108.115153> for the detailed computational methods; spinless two-band TB models of SG 113, SG 128, and SG 53; analysis of the 2NS+QNL phonon in C<sub>4</sub>N; material candidates for ideal two-band NS+NL phonons; and four-band situations of NS+NL phonons and their material candidates. The Supplemental Material also contains Refs. [44–47].
- [44] G. Kresse and J. Furthmüller, *Phys. Rev. B* **54**, 11169 (1996).
- [45] J. P. Perdew, K. Burke, and M. Ernzerhof, *Phys. Rev. Lett.* **77**, 3865 (1996).
- [46] M. López-Sancho, J. Lopez Sancho, and J. Rubio, *J. Phys. F* **15**, 851 (2000).
- [47] Q.-S. Wu, S. Zhang, H. Song, M. Troyer, and A. Soluyanov, *Comput. Phys. Commun.* **345**, 224 (2017).
- [48] J.-T. Wang, S. Nie, H. Weng, Y. Kawazoe, and C. Chen, *Phys. Rev. Lett.* **120**, 026402 (2018).
- [49] A. Jain, S. P. Ong, G. Hautier, W. Chen, W. D. Richards, S. Dacek, S. Cholia, D. Gunter, D. Skinner, G. Ceder *et al.*, *APL Mater.* **1**, 011002 (2013).
- [50] A. Togo and I. Tanaka, *Scr. Mater.* **108**, 1 (2015).
- [51] S. Baroni, S. de Gironcoli, A. Dal Corso, and P. Giannozzi, *Rev. Mod. Phys.* **73**, 515 (2001).
- [52] Z. Shi, W. Shao, L. Rao, X. Xing, Y. Zhou, X. Ren, and Q. Yang, *Phys. Chem. Chem. Phys.* **24**, 5171 (2022).
- [53] C. Zhong, Y. Chen, Y. Xie, S. A. Yang, M. L. Cohen, and S. B. Zhang, *Nanoscale* **8**, 7232 (2016).
- [54] Y. X. Zhao and Z. D. Wang, *Phys. Rev. B* **89**, 075111 (2014).
- [55] Y. H. Chan, C.-K. Chiu, M. Y. Chou, and A. P. Schnyder, *Phys. Rev. B* **93**, 205132 (2016).
- [56] J. Zak, *Phys. Rev. Lett.* **62**, 2747 (1989).
- [57] P. Delplace, D. Ullmo, and G. Montambaux, *Phys. Rev. B* **84**, 195452 (2011).
- [58] G. Thiele, C. Mrozek, D. Kämmerer, and K. Wittmann, *Z. Naturforsch. B* **38**, 905 (1983).
- [59] H.-J. Deiseroth, M. Wagener, and E. Neumann, *Eur. J. Inorg. Chem.* **2004**, 4755 (2004).
- [60] M. D. Smith and G. J. Miller, *J. Am. Chem. Soc.* **118**, 12238 (1996).
- [61] J. Gong, J. Wang, H. Yuan, Z. Zhang, W. Wang, and X. Wang, *Phys. Rev. B* **106**, 214317 (2022).
- [62] J. Wang, H. Yuan, Z.-M. Yu, Z. Zhang, and X. Wang, *Phys. Rev. Mater.* **5**, 124203 (2021).
- [63] G. Liu, Z. Chen, P. Wu, and H. Xu, *Phys. Rev. B* **106**, 214308 (2022).
- [64] X. Wang, F. Zhou, Z. Zhang, Z.-M. Yu, and Y. Yao, *Phys. Rev. B* **106**, 214309 (2022).
- [65] B. Zheng, F. Zhan, X. Wu, R. Wang, and J. Fan, *Phys. Rev. B* **104**, L060301 (2021).
- [66] Y. Xu, M. G. Vergniory, D.-S. Ma, J. L. Mañes, Z.-D. Song, B. A. Bernevig, N. Regnault, and L. Elcoro, [arXiv:2211.11776](https://arxiv.org/abs/2211.11776).
- [67] J. Li, J. Liu, S. A. Baronett, M. Liu, L. Wang, R. Li, Y. Chen, D. Li, Q. Zhu, and X.-Q. Chen, *Nat. Commun.* **12**, 1204 (2021).

- [68] S. Singh, Q. S. Wu, C. Yue, A. H. Romero, and A. A. Soluyanov, *Phys. Rev. Mater.* **2**, 114204 (2018).
- [69] Z. Chen, X. Zhang, and Y. Pei, *Adv. Mater.* **30**, 1705617 (2018).
- [70] T. Zhang, Z. Song, A. Alexandradinata, H. Weng, C. Fang, L. Lu, and Z. Fang, *Phys. Rev. Lett.* **120**, 016401 (2018).
- [71] W.-H. Dong, Y.-Y. Zhang, Y.-F. Zhang, J.-T. Sun, F. Liu, and S. Du, *NPJ Comput. Mater.* **8**, 185 (2022).
- [72] S. Zhang, J. Guan, X. Jia, B. Liu, W. Wang, F. Li, L. Wang, X. Ma, Q. Xue, J. Zhang *et al.*, *Phys. Rev. B* **94**, 081116(R) (2016).
- [73] H. He, C. Qiu, L. Ye, X. Cai, X. Fan, M. Ke, F. Zhang, and Z. Liu, *Nature (London)* **560**, 61 (2018).
- [74] M. Wang, W. Zhou, L. Bi, C. Qiu, M. Ke, and Z. Liu, *Nat. Commun.* **11**, 3000 (2020).
- [75] Z. Zhang, Y. Tian, Y. Wang, S. Gao, Y. Cheng, X. Liu, and J. Christensen, *Adv. Mater.* **30**, 1803229 (2018).
- [76] T. T. Zhang, H. Miao, Q. Wang, J. Q. Lin, Y. Cao, G. Fabbris, A. H. Said, X. Liu, H. C. Lei, Z. Fang *et al.*, *Phys. Rev. Lett.* **123**, 245302 (2019).
- [77] H. Miao, T. T. Zhang, L. Wang, D. Meyers, A. H. Said, Y. L. Wang, Y. G. Shi, H. M. Weng, Z. Fang, and M. P. M. Dean, *Phys. Rev. Lett.* **121**, 035302 (2018).
- [78] I.-H. Lee, D. Yoo, P. Avouris, T. Low, and S.-H. Oh, *Nat. Nanotechnol.* **14**, 313 (2019).
- [79] F. Thouin, D. A. Valverde-Chávez, C. Quarti, D. Cortecchia, I. Bargigia, D. Beljonne, A. Petrozza, C. Silva, and A. R. Srimath Kandada, *Nat. Mater.* **18**, 349 (2019).
- [80] R. M. Pettit, W. Ge, P. Kumar, D. R. Luntz-Martin, J. T. Schultz, L. P. Neukirch, M. Bhattacharya, and A. N. Vamivakas, *Nat. Photon.* **13**, 402 (2019).
- [81] F. S. Hage, D. M. Kepaptsoglou, Q. M. Ramasse, and L. J. Allen, *Phys. Rev. Lett.* **122**, 016103 (2019).